Anomalous strain-energy-driven macroscale translation of grains during non-isothermal annealing

M.J. Higgins[1], J. Kang[2], G. Huang[1], D. Montiel[1], N. Lu[1], H. Liu[3], Y-F. Shen[3], P. Staublin[4], J.-S. Park[5], J.D. Almer[5], P. Kenesei[5], P.G. Sanders[4], R.M. Suter[3], K. Thornton[1], and A.J. Shahani[1]

1 Department of Materials Science and Engineering, University of Michigan, Ann Arbor, MI 48019, USA

2 Department of Chemical Engineering, University of Michigan, Ann Arbor, Michigan, 48109, USA

3 Department of Physics, Carnegie Mellon University, Pittsburgh, PA 15213, USA

4 Department of Materials Science & Engineering, Michigan Technological University, Houghton, MI 49931-1295, USA

5 X-ray Science Division, Advanced Photon Source, Argonne National Laboratory, Lemont, Illinois 60439, USA

48019, USA

*Corresponding author: Ashwin J. Shahani: shahani@umich.edu, +1 734 764 5648

We report a new mode of grain growth, involving the macroscopic translation of grain centers during non-isothermal annealing. Through synchrotron high-energy x-ray diffraction microscopy, we find dissolution of semi-coherent precipitates generates dislocations, thereby raising the stored strain energy within grains. The subsequent evolution of grains shows unexpected grain translations over length scales of 10-100 μm. Phase-field simulations reveal that such translations are not uncommon in strain-energy-driven grain growth, wherein different regions of a grain may grow and shrink simultaneously.

A wide range of physical systems are composed of domains of different crystallographic orientation, from dusty plasmas[1] to colloidal crystals[2] to polycrystalline metals[3,4]. Our traditional understanding is that the domains (hereafter called grains) will grow and shrink in response to the capillary pressure across their boundaries. That is, a grain boundary (GB) migrates towards its center of curvature with a velocity, v, proportional to the pressure, P_g, as $v = MP_g$ where M is a

phenomenological, temperature-dependent grain boundary mobility and P_g is taken to be the product of the local mean curvature, H, and the grain boundary energy, γ_{gb}. This capillary-driven growth law has found success in explaining the evolution of bubbles in soap froths[5,6,7,8,9]. More refined models of grain boundary displacement do consider the driving force due to the long-range interactions between disconnections along the grain boundary[10]. However, these descriptions are insufficient to fully explain the richness in grain growth dynamics[11,12,13]. This is mainly because they do not take into account many other confounding factors that perturb the GB trajectories such as spatial variation in densities of bulk dislocations and second-phase precipitates[14,15,16,17].

As an example, Omori et al.[18] and Kusama et al.[19] observed the development of subgrain structures in Cu-Al-Mn alloys during dynamic annealing, *i.e.*, oscillating above and below the solvus temperature for the FCC-α phase. They proposed that these subgrain structures accommodate transformational strains between the FCC particles and BCC matrix *via* geometrically necessary dislocations, which presumably provide an energetic advantage for GBs to migrate. It stands to reason that stored strain energy may lead to a significant displacement of grain centers (in addition to grain growth and shrinkage), although this phenomenon has yet to be explored in detail. To our knowledge, past studies focused on grain displacement *via* grain boundary coupling and sliding driven by externally applied stresses[20,21] or as a consequence of artificially introduced chemical potential gradients in a multi-phase system[22]. None have experimentally observed this phenomenon nor attributed it directly to stored strain energy. The microstructural consequences of a stored strain energy (in the absence of an external stress) remain an enigma, in part due to the lack of a suitable model to quantitatively study the effect of the driving force arising from dislocation density when it varies from a grain to grain and/or within each of the grains. Moreover, it is impossible to reconstruct the interfacial dynamics underlying grain growth through a *post mortem* characterization of microstructure. Recent expansions of *in situ* characterization capabilities at synchrotron facilities offer unparalleled insights into microstructural evolution[23,24,25].

In this Letter, we reveal a new mechanism of grain growth, whereby an entire grain effectively migrates with the aid of an elevated and inhomogeneous lattice strain. This discovery was made possible through synchrotron high energy x-ray diffraction microscopy (HEDM)[23,26,27,28] coupled to an *in situ* furnace (see Supplementary Information). We resolve the microstructural details during dynamic, non-isothermal annealing with spatial and angular resolutions of 1 μm and 0.1°,

respectively. The resolvable unit in HEDM is the individual pixel/voxel, compared to a much larger discretization unit (the entire grain) in diffraction contrast x-ray tomography (DCT)[29,30]. This attribute makes HEDM the ideal tool for capturing lattice rotations within each grain, and in turn, the dislocation densities. Analysis of dislocation densities calculated from near-field (NF) HEDM reconstructions shows the apparent distance traversed by a grain is of the same order as the grain size (10-100 μm) when the mean and variance in coarse-grained dislocation densities are of the order 10^{13} and 10^{12} m^{-2}, respectively, and temperature is adequately high to drive grain growth (≥650°C). To fill in the spatiotemporal gaps of our experiment, we conduct phase-field simulations of grain growth incorporating an additional driving force from the stored energy due to the presence of dislocations. Our joint experiment and simulation provide a unified description of the mechanism of grain translation.

We investigate grain growth in Cu-Al-Mn as a model system, following the work of Kusama et al.[19]. An ingot of composition Cu-17at%Al-11.4at%Mn was machined in the shape of cylindrical rods of 1mm diameter by 7cm height. The grain structure of the prepared samples was equiaxed with a grain size of 79.7μm; the GB distribution was near-random; and the crystallographic texture was weak (see Supplementary Information). HEDM experiments were conducted at beam-line 1-ID-E at the Advanced Photon Source at Argonne National Laboratory. Orientations in each quasi-two-dimensional sample slice probed by the beam were optimized on a square array of points with 7 μm spacing and spanning the 1mm diameter circular sample cross-section. Slices separated by a distance of 7 μm were concatenated to yield a three-dimensional volume. Of note is that a new NF-HEDM compatible infrared furnace was mounted at the beamline for the first time (**Fig. S3**), allowing for *in situ* imaging of diffraction signals while avoiding the challenges associated with alignment of a sequence of volumetric data sets.

Samples were subjected to a dynamic annealing schedule similar to the 'low temperature cycle' described by Kusama et al[19]. A given cycle begins with a 5min. hold at 260°C and ends when the sample is quenched immediately upon heating to a temperature just above the α solvus (726°C); see Supplementary Information. One cycle of dynamic annealing was completed before imaging the second cycle at the following temperature points: 505°C, 650°C, and 730°C. We conducted our study in an 'interrupted *in situ*' manner,[31] whereby the sample was air quenched after reaching the prescribed temperature and subsequently imaged at room temperature. HEDM data collected

after the 730°C anneal has inter-layer spacing of 43 μm to accommodate the significant increase in grain size. Reconstructed 2D (slice) and 3D (volumetric) data were processed and analyzed in MATLAB using the *PolyProc* function package[32] (see Supplementary Information). Diffraction spots from the BCC-β phase were tracked over time and found to be largely preserved during thermal cycling.

Fig. 1(a) shows grain maps of two datasets labelled S_1 and S_2 and collected after annealing at 650°C and 730°C, respectively. Datasets are shown with specimen $\hat{z}$ axis through the page for better viewing of the underlying grain structure. The circular silhouette represents the external sample surfaces. The FCC particles that are present within the grains are not shown here, as our focus is on the evolution of the grain structure. It is important to note that the imaging field-of-view (FOV) represents an open system: grains are free to move into and out of the FOV from its top and bottom surfaces (i.e., into and out of the page in **Fig. 1(a)**). That is, the length of the cylinder

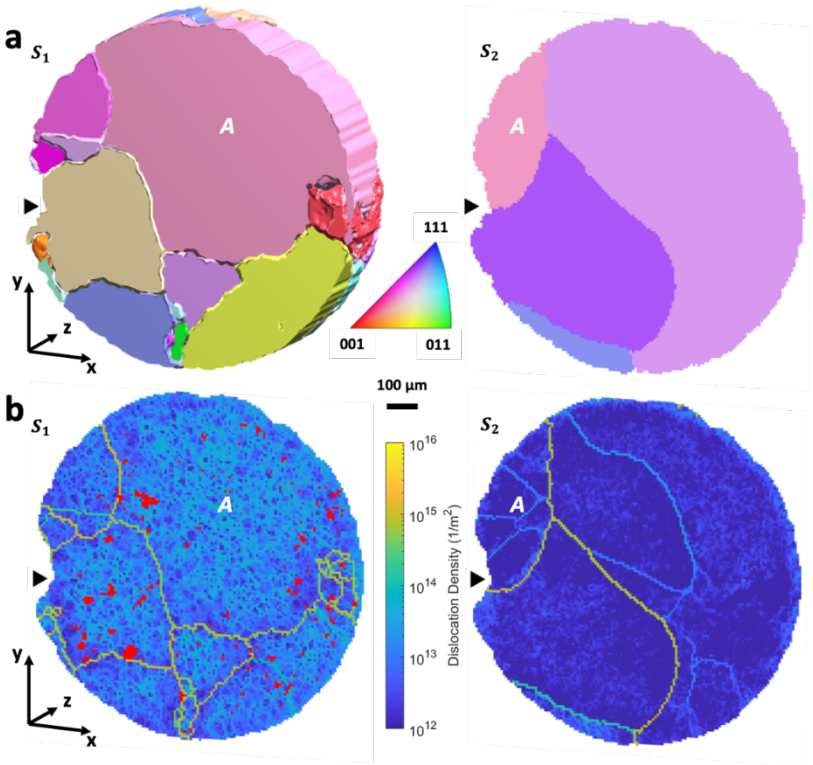

Fig. 1. (a) Grain maps at 650°C (S_1, left) and 730°C (S_2, right) colored based on the inverse pole figure relative to the specimen $\hat{z}$ axis. Reconstructed datasets are displayed at an azimuth angle of 20° and an elevation of 10° for perspective. Grain *A* undergoes significant displacement and is marked for reference. Particles are excluded for clarity. (b) Dislocation density maps in cross-section of states S_1 (left) and S_2 (right) with grain *A* indicated. Yellow regions correspond to high dislocation density and blue the converse. Red regions represent α particles. Arrow points to a notch used for sample alignment.

sample is much larger than the length of the FOV (along the specimen $\hat{z}$ direction). It is also worth noting that the two datasets are aligned in the $\hat{x} - \hat{y}$ plane, with the silhouette of the sample matching exactly (see arrows pointing to fiducial notch on the left-hand-side). While we find a slight misalignment of 14 μm along the $\hat{z}$ axis, it is relatively minor considering the scale of the grains (average equivalent radii of 90 grains at S_1 is 112 μm), and, as we will see, their displacement (comparable to the grain size). We follow the evolution of the grain labelled *A* between the temperatures of 650°C (S_1) and 730°C (S_2), which is the largest grain visible in the imaging FOV. Over the course of 800 minutes from states S_1 to S_2, grain *A* shrinks significantly (from 273 to 168 μm) and its center has translated across the FOV by 70 μm. This behavior upends our conventional wisdom of capillary-driven abnormal grain growth[33], wherein the largest grains with the most grain neighbors (such as *A*) are expected to grow out and consume the sample volume[32,34]. Moreover, the self-similar nature of capillary-driven grain growth results in significant back pressure from neighboring grains[35,36,37], which would prohibit significant displacements of grain centers. Clearly, a new mechanism is required to explain the observation.

We postulate that the observed center translation and size reduction of grain *A* are due to the differences in stored strain energy between the grains (**Fig. 1(b)**), resulting from the dislocations

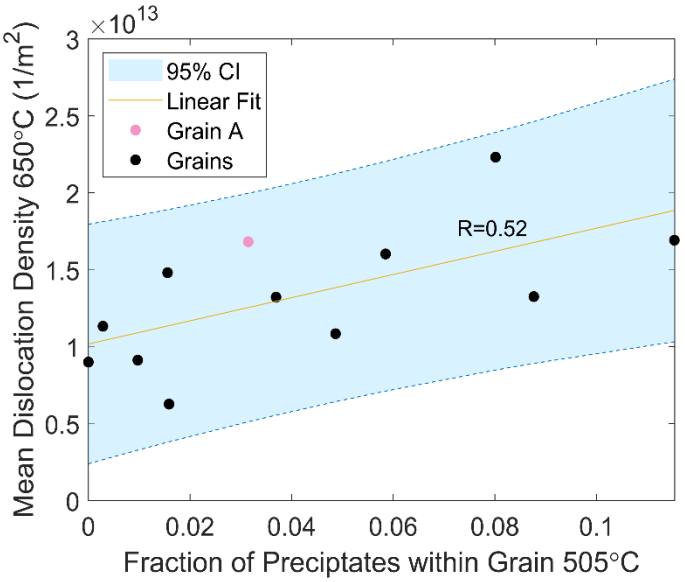

Fig. 2. Mean dislocation density averaged over each grain at 650°C *vs.* the volume fraction of α precipitates within the grain at 505°C (α solvus: 726°C), showing a positive correlation. Each point represents one grain tracked between the two datasets. Grain *A* is indicated for reference. A linear fit with Pearson correlation coefficient of 0.52 is shown, along with 95% confidence interval bounds.

generated by the semi-coherent BCC-β−FCC-α interface upon dissolution of α phase. In this case, grains that contain a higher density of α precipitates should possess a correspondingly higher dislocation density. To confirm this hypothesis, we plot the grain-averaged dislocation density against the particle density at the preceding temperature point (505°C). **Fig. 2** shows a scattered but clearly positive correlation between the two quantities. Within grains, the generated dislocations form cellular subgrain structures as seen in the S_1 dataset of **Fig. 1(b)**. Subgrain structures have a misorientation <5° with respect to the grain-averaged orientation (by definition[38]) and represent dislocation densities within the grains. Since precipitate density varies from grain to grain, as well as within a grain, dynamic annealing leads to a corresponding spatial variation in dislocation density and thus in stored strain energy. Annealing between the S_1 and S_2 states leads to a drop in the dislocation density by one order-of-magnitude on average due to recovery and grain growth; see **Fig. 1(b)**. The volume fraction of α phase also decreases from 0.14 to near-zero between the two temperature points, as expected. The evolution of the grain structure from S_1 to S_2 is marked by the shrinkage and, in extreme cases, disappearance of grains with high stored strain energies in S_1. We note also there is no preferential texture at the S_2 state (see also **Fig. S6**) nor is there any evidence of "particle stimulated nucleation of recrystallization"[39].

The high fidelity of the HEDM data enables us to calculate and compare the various driving forces for GB motion, including capillarity and stored energy. Taking γ_{gb} to be 0.595 J/m^2 from Kusama et al.[19] and calculating the surface-weighted mean curvature[40,41] $\overline{H}$ of grain A directly from the 3D reconstruction to be $(4.3 \pm 0.2) \times 10^3$ m^{-1}, the capillary pressure $\gamma_{gb}\overline{H}$ is 2.6 ± 0.1 kPa. Meanwhile, the stored strain energy, $f_{stored}(\vec{r})$ at point $\vec{r}$, is[38,42]

$$f_{stored}(\vec{r}) = \frac{1}{2} G b^2 \rho(\vec{r}), \quad (1)$$

where G is the shear modulus of β phase at a temperature of 650°C assuming isotropic, elastic behavior, 28.3GPa;[43] b is the magnitude of the Burger's vector, 0.255 nm; and ρ is the dislocation density. From the difference in ρ between grain A and its grain neighbors in the S_1 state in **Fig. 1**, which was determined to be $(5.7 \pm 3.1) \times 10^{12}$m^{-2}, the corresponding driving pressure due to stored strain energy is calculated to be 5.2 ± 2.8 kPa. Thus, the driving pressures associated with capillarity and stored strain energy are of the same order of magnitude. We also consider the influence of the precipitates and external surfaces on retarding grain growth. According to classical

measures,[44] the particle drag pressure should decay to zero as the volume fraction of particles approaches zero (**Fig. 1(b)**). Likewise, the pressure associated with GB groove pinning[38,45] is about one order of magnitude smaller than the pressure associated with the stored strain energy. Thus, stored strain energy plays an important role in driving grain growth, largely unhindered by the particle drag near the solvus temperature.

To help interpret our results and provide insight in microstructural evolution between the two end states, we developed a phase-field model[46,47,48,49] that extends the recrystallization model employed by Moelans et al.[50,51] and Gentry et al.,[52,53] which accounts for the contribution of strain energy to the driving pressure for GB displacement, $f_{stored}(\vec{r},t)$ in Eq. (1). We approximate the local dislocation density $\rho(\vec{r},t)$ in a system of N grains as a weighted average of the dislocation density of each grain, ρ_i, which is assumed to be uniform in the bulk and constant in time:

$$\rho(\{\eta_i(\vec{r},t)\}) = \frac{\sum_{i=1}^{N}\eta_i^2\rho_i}{\sum_{i=1}^{N}\eta_i^2}, \tag{2}$$

where $\eta_i(\vec{r},t)$ represents the order parameter of the i-th grain, which is a field having a value of 1 within the grain and 0 outside. The time-evolution of each of the order parameters is driven by the reduction of the free energy as described by Allen-Cahn dynamics,

$$\frac{\partial\eta_i}{\partial t} = -L\left(\frac{\delta F}{\delta\eta_i}\right), \tag{3}$$

while the governing equation for the dislocation density field is given by

$$\frac{\partial\rho}{\partial t} = \frac{\left[\sum_{i=1}^{N}\left(2\eta_i\frac{\partial\eta_i}{\partial t}\rho_i\right)\right](\sum_{i=1}^{N}\eta_i^2) - \left[\sum_{i=1}^{N}\left(2\eta_i\frac{\partial\eta_i}{\partial t}\right)\right][\sum_{i=1}^{N}(\eta_i^2\rho_i)]}{[\sum_{i=1}^{N}\eta_i^2]^2} \tag{4}$$

See Supplementary Information for the full derivation of the model.

We employ the model described above to simulate two scenarios of grain growth: with and without the effect of stored energy. The system is set up to initially contain 80 grains (see the Supplementary Information for the generation of the initial condition), as shown in **Fig. 3(a)**. For the simulation with stored energy, the dislocation density values were chosen randomly from a normal distribution with mean of $1.21 \times 10^{13}\text{m}^{-2}$ and standard deviation of $3.8 \times 10^{12}\text{m}^{-2}$ based on the experimental results from the S_1 state (see **Fig. S7**). The intermediate and final states are

defined to be the states that contain 77 and 69 grains, respectively. Microstructure evolution that considers the stored energy is shown in **Figs. 3(b)-(c)**. For comparison, grain growth that does not consider the contribution of stored energy is presented in **Figs. 3(e)-(f)**, in which the same set of colors is used to indicate different grains. Even though capillary-driven grain growth occurs in both cases, for the strain-driven case, it can be observed that the grain boundary motion is primarily driven by the differences in the stored strain energy between neighboring grains, leading to grain boundary migration toward regions with lower dislocation density. A grain with a medium value of dislocation density may grow into a neighboring grain with higher value and at the same time be consumed by another neighboring grain with low value on the opposite side; the net result is a large-scale translation of the grain. Two examples are highlighted by the grains marked by A and B in **Fig. 3(a)-(c)**, whose positions of grain boundaries at $t^* = 0$, 250, and 500 are indicated in blue, green and red, shown in **Fig. 3(g)**. The translation of the grains is evidenced by the small degree of overlap between the initial and final regions, which was the criterion used in the selection

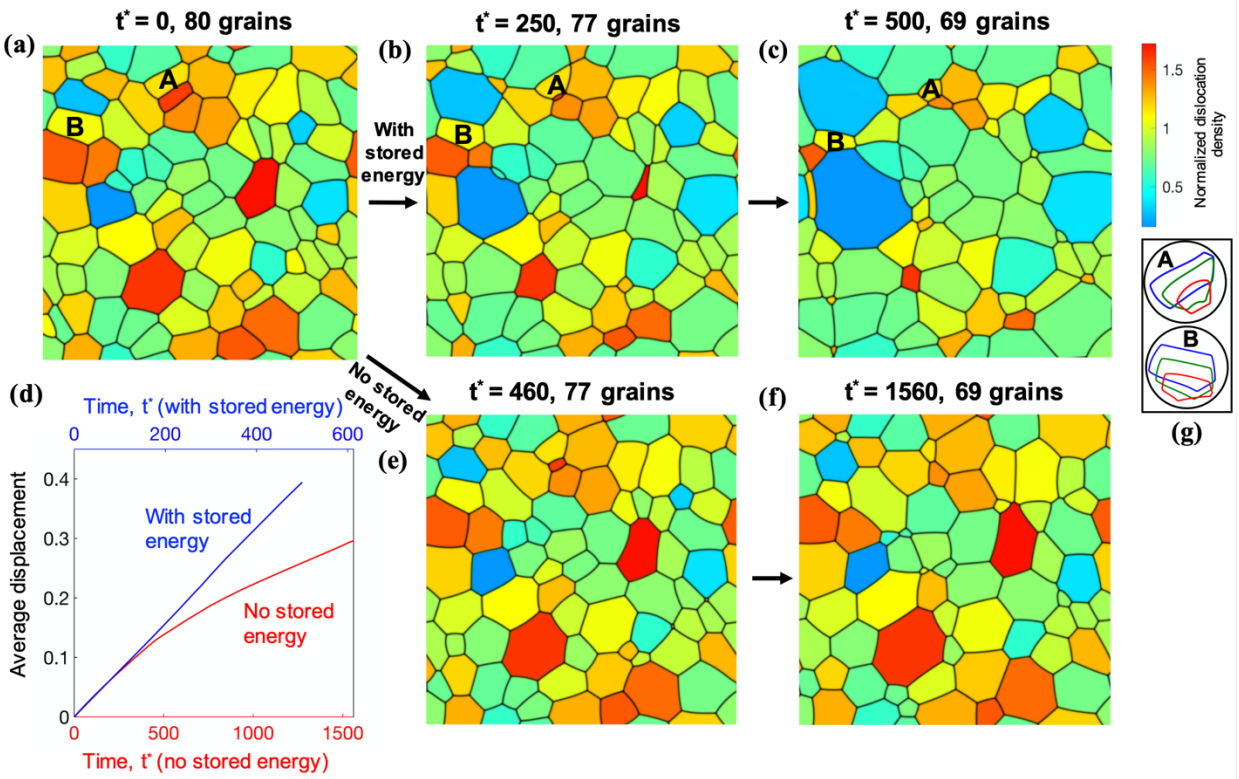

Fig. 3. Phase-field simulations of grain growth. (a) Initial arrangements of the grains. (b) Intermediate state with 77 grains and (c) final state with 69 grains (with a stored energy term). (e) Intermediate state with 77 grains and (f) final state with 69 grains (without stored energy term). (d) Average displacement of the grains' center of mass. The time axis of the capillary-driven case is rescaled so that two curves visually have the same initial slope. (g) Translations of grains A and B. Blue, green and red outlines indicate the positions of GBs at time $t^* = 0$, 250 and 500, respectively, of the two grains. Dislocation density shown in the figures is normalized with respect to the mean (1.25×10^{13}m^{-2}) of the dislocation densities of the grains in the initial condition. Color indicates the normalized dislocation density where the stored energy is considered (a-c) and indicates different grains otherwise.

of these grains (more details are provided in the Supplementary Information). Moreover, while the small computational domain size does not permit a quantitative analysis, the simulation demonstrates that strain-energy-driven grain growth results in a grain size distribution having extreme values (**Fig. 3(c)**, where more small and large grains emerge as compared to the capillary-driven grain growth shown in **Fig. 3(f)**). The comparison of the grain size distribution for the systems with 50 remaining grains is provided in the Supplementary Information (see **Fig. S8**). The strain-energy-driven grain growth appears to be leading to a grain microstructure with a bimodal distribution, which is one of the classic signatures of abnormal grain growth[38,54,55].

To quantitatively compare the grain translation in the two cases, we compute the magnitude of the displacement of each grain's center of mass as a function of time. We plot the average displacement of the center-of-mass positions of the grains at different time, as shown in **Fig. 3(d)**. The grains that disappear during the evolution are included in this average using their displacement at their final value. The unit length for the displacement is assumed to be 128μm, the average grain radius estimated from the experiment, and t^* is a nondimensionalized time (see Supplementary Information). The time axis of the capillary-driven case is rescaled so that the initial slopes (the rate of change of the average displacement) of two curves are visually matched. Although the magnitudes of the average displacement of two cases are comparable at the start of the simulation, the average displacement in the strain-energy-driven simulation maintains a higher rate than in the capillary-driven simulation. The latter is driven solely by the reduction of the system's total grain boundary energy (that scales as $t^{-1/2}$)[56].

Our observations are somewhat reminiscent of the so-called "grain migrations" seen in dynamic recrystallization[57] and grain boundary sliding *via* Rachinger[58,59] and Lifshitz mechanisms[60,61]. Yet the underlying mechanisms are fundamentally different. In those cases, lattice defect energy is continuously being supplied to the grains by the deformation, and the grains will move along the direction of the applied stress. In contrast, our sample was fully recrystallized prior to annealing to ensure the residual stored strain energy from rolling was eliminated (see **Fig. S1**). Furthermore, it was not subjected to any plastic deformation during the anneal cycle. That is, in our case, dislocations are embedded by thermal processing (see **Fig. S4** and **Fig. 2**) and not mechanical processing. The geometrically necessary dislocations can be re-introduced with additional anneal cycles, thereby stimulating strain-energy-driven (abnormal) grain growth. Nevertheless, our

simulations show that the driving force from the stored energy reduces with time (see **Fig. 3c**, where most of the high-dislocation-density regions have been eliminated, and **Fig. S9** showing the driving forces as a function of time), which explains why cyclic heat treatment is necessary in driving abnormal grain growth. The phase field model developed herein will offer an understanding of how the stored-energy driving force evolves with time and how to optimize such a process to achieve polycrystalline microstructures with exceptionally large grains, given the rate of dislocation formation during non-isothermal heat treatment.

In summary, we have investigated the translation of grain centers during non-isothermal annealing. HEDM together with an *in situ* furnace enabled us to characterize not only the two-phase microstructures but also dislocation densities within each grain. Our results support the hypothesis that differences in dislocation densities between grains induce their apparent translation. Phase-field simulations demonstrate that grains with lower strain energy grew in expense of those with higher strain energy, resulting in a decrease in stored energy. The process of grain growth is highly inhomogeneous and localized, with some grain boundaries growing outward and others receding inwards. Our integrated efforts show that stored strain energy and its gradient bring about a complexity in the dynamical behavior of polycrystals, not predicted by conventional theories of grain growth nor detected through *post mortem* metallographic analyses. These results have broader implications to systems with stored energy differences between neighboring grains from other sources, such as an elastic or magnetic anisotropy[62,63], where grain translations may be expected to occur.

We acknowledge support from the National Science Foundation under Award No. DMR-2003719. This research used resources of the Advanced Photon Source, a U.S. Department of Energy (DOE) Office of Science User Facility operated for the DOE Office of Science by Argonne National Laboratory under Contract No. DE-AC02-06CH11357. Computational resources and services were provided by the Extreme Science and Engineering Discovery Environment (XSEDE) through allocation TG-DMR110007. David Montiel was supported by the U.S. Department of Energy, Office of Basic Energy Sciences, Division of Materials Sciences and Engineering under Award no. DE-SC0008637 that funds the Center for PRedictive Integrated Structural Materials Science (PRISMS Center) at the University of Michigan. The authors acknowledge the Michigan Center for Materials Characterization $(MC)^2$ for use of the instruments. Work at Carnegie Mellon was

supported in part by the National Science Foundation under grant DMR-1628994 and in part by Department of Energy grant NA0003915.

References

1. Chan, C. L., Woon, W. Y. & Lin, I. Shear banding in mesoscopic dusty plasma liquids. *Phys. Rev. Lett.* **93**, 1–4 (2004).
2. Pertsinidis, A. & Ling, X. S. Statics and dynamics of 2D colloidal crystals in a random pinning potential. *Phys. Rev. Lett.* **100**, 2–5 (2008).
3. Kadau, K. *et al.* Shock waves in polycrystalline iron. *Phys. Rev. Lett.* **98**, 1–4 (2007).
4. Barmak, K. *et al.* Grain growth and the puzzle of its stagnation in thin films: The curious tale of a tail and an ear. *Prog. Mater. Sci.* **58**, 987–1055 (2013).
5. Kraynik, A. M., Koehler, S. A., Stone, H. A. & Hilgenfeldt, S. An accurate von Neumann's law for three-dimensional foams. *Phys. Rev. Lett.* **86**, 2685–2688 (2001).
6. Kraynik, A. M., Reinelt, D. A. & van Swol, F. Structure of random monodisperse foam. *Phys. Rev. E - Stat. Physics, Plasmas, Fluids, Relat. Interdiscip. Top.* **67**, 11 (2003).
7. Cox, S. J. & Fortes, M. A. Properties of three-dimensional bubbles of constant mean curvature. *Philos. Mag. Lett.* **83**, 281–293 (2003).
8. Hilgenfeldt, S., Kraynik, A. M., Reinelt, D. A. & Sullivan, J. M. The structure of foam cells: Isotropic Plateau polyhedra. *Europhys. Lett.* **67**, 484–490 (2004).
9. Kraynik, A. M., Reinelt, D. A. & Van Swol, F. Structure of random foam. *Phys. Rev. Lett.* **93**, 1–4 (2004).
10. Zhang, L., Han, J., Xiang, Y. & Srolovitz, D. J. Equation of Motion for a Grain Boundary. *Phys. Rev. Lett.* **119**, 1–5 (2017).
11. Shen, Y. F. *et al.* Importance of outliers: A three-dimensional study of coarsening in α - phase iron. *Phys. Rev. Mater.* **3**, 1–13 (2019).
12. Bhattacharya, A. *et al.* Three-dimensional observations of grain volume changes during annealing of polycrystalline Ni. *Acta Mater.* **167**, 40–50 (2019).
13. Zhang, J. *et al.* Grain boundary mobilities in polycrystals. *Acta Mater.* **191**, 211–220 (2020).
14. Zhang, K., Weertman, J. R. & Eastman, J. A. Rapid stress-driven grain coarsening in nanocrystalline Cu at ambient and cryogenic temperatures. *Appl. Phys. Lett.* **87**, 1–4 (2005).
15. Jin, M., Minor, A. M., Stach, E. A. & Morris, J. W. Direct observation of deformation-induced grain growth during the nanoindentation of ultrafine-grained Al at room temperature. *Acta Mater.* **52**, 5381–5387 (2004).
16. Mompiou, F., Legros, M. & Caillard, D. Stress assisted grain growth in ultrafine and nanocrystalline aluminum revealed by in-situ TEM. *Mater. Res. Soc. Symp. Proc.* **1086**, 19–24 (2008).
17. Legros, M., Gianola, D. S. & Hemker, K. J. In situ TEM observations of fast grain-boundary motion in stressed nanocrystalline aluminum films. *Acta Mater.* **56**, 3380–3393 (2008).
18. Omori, T. *et al.* Abnormal Grain Growth Induced by Cyclic Heat Treatment. *Science* **341**, 1500–1503 (2013).
19. Kusama, T. *et al.* Ultra-large single crystals by abnormal grain growth. *Nat. Commun.* **8**, 1–8 (2017).

20. Cahn, J. W. & Taylor, J. E. A unified approach to motion of grain boundaries, relative tangential translation along grain boundaries, and grain rotation. *Acta Mater.* **52**, 4887–4898 (2004).
21. Thomas, S. L., Chen, K., Han, J., Purohit, P. K. & Srolovitz, D. J. Reconciling grain growth and shear-coupled grain boundary migration. *Nat. Commun.* **8**, 1–12 (2017).
22. Salvalaglio, M., Srolovitz, D. J. & Han, J. Disconnection-Mediated Migration of Interfaces in Microstructures: II. diffuse interface simulations. *arXiv Prepr. arXiv ID 2103.09688* (2021).
23. Bernier, J. V., Suter, R. M., Rollett, A. D. & Almer, J. D. High-Energy X-Ray Diffraction Microscopy in Materials Science. *Annu. Rev. Mater. Res.* **50**, 395–436 (2020).
24. Withers, P. J. Synchrotron X-ray Diffraction. in *Practical Residual Stress Measurement Methods* (ed. Schajer, G.) 163–194 (2013).
25. Shahani, A. J., Xiao, X., Lauridsen, E. M. & Voorhees, P. W. Characterization of metals in four dimensions. *Mater. Res. Lett.* **8**, 462–476 (2020).
26. Hefferan, C. M., Li, S. F., Lind, J. & Suter, R. M. Tests of microstructure reconstruction by forward modeling of high energy X-ray diffraction microscopy data. *Powder Diffr.* **25**, 132–137 (2010).
27. Li, S. F. & Suter, R. M. Adaptive reconstruction method for three-dimensional orientation imaging. *J. Appl. Crystallogr.* **46**, 512–524 (2013).
28. Suter, R. M., Hennessy, D., Xiao, C. & Lienert, U. Forward modeling method for microstructure reconstruction using x-ray diffraction microscopy: Single-crystal verification. *Rev. Sci. Instrum.* **77**, 123905 (2006).
29. Ludwig, W. *et al.* Three-dimensional grain mapping by x-ray diffraction contrast tomography and the use of Friedel pairs in diffraction data analysis. *Rev. Sci. Instrum.* **80**, 033905 (2009).
30. Bachmann, F., Bale, H., Gueninchault, N., Holzner, C. & Lauridsen, E. M. 3D grain reconstruction from laboratory diffraction contrast tomography. *J. Appl. Crystallogr.* **52**, 643–651 (2019).
31. Patterson, B. M., Cordes, N. L., Henderson, K., Xiao, X. & Chawla, N. Data Challenges of In-situ X-ray Tomography for Materials Discovery and Characterization. *Springer* 129–165 (2018).
32. Lu, N. *et al.* Dynamics of particle-assisted abnormal grain growth revealed through integrated three-dimensional microanalysis. *Acta Mater.* **195**, 1–12 (2020).
33. Andersen, I. & Grong, Ø. Analytical Modelling of Grain Growth in Metals and Alloys in the Presence of Growing and Dissolving Precipitates - I. Normal Grain Growth. *Acta Metall.* **43**, 2673–2688 (1995).
34. Rios, P. R. & Glicksman, M. E. Topological theory of abnormal grain growth. *Acta Mater.* **54**, 5313–5321 (2006).
35. Rios, P. R., Gottstein, G. & Shvindlerman, L. S. An irreversible thermodynamic approach to normal grain growth with a pinning force. *Mater. Sci. Eng. A* **332**, 231–235 (2002).
36. Mullins, W. W. The statistical self-similarity hypothesis in grain growth and particle coarsening. *J. Appl. Phys.* **59**, 1341–1349 (1986).
37. Gottstein, G., Rollett, A. D. & Shvindlerman, L. S. On the validity of the von Neumann-Mullins relation. *Scr. Mater.* **51**, 611–616 (2004).
38. Rollett, A., Humphreys, F., Rohrer, G. S. & Hatherly, M. *Recrystallization and Related Annealing Phenomena: Second Edition*. *Recrystallization and Related Annealing*

Phenomena: Second Edition (2004).
39. Lei, X. *et al.* Particle stimulated nucleation revisited in three dimensions: a laboratory-based multimodal X-ray tomography investigation. *Mater. Res. Lett.* **9**, 65–70 (2021).
40. Cahn, J. W. Significance of average mean curvature and its determination by quantitative metallography. *Trans. Metall. Soc. AIME* **239**, 610 (1967).
41. DeHoff, R. T. Quantitative estimation of mean surface curvature. *Trans. Metall. Soc. AIME* **239**, 617 (1967).
42. Boulais-Sinou, R. *et al.* Full field modeling of dynamic recrystallization in a global level set framework, application to 304L stainless steel. *MATEC Web Conf.* **80**, 02005 (2016).
43. Pettersson, B. The stacking-fault energy in CuMn and CuAlMn alloys. *Philos. Mag.* **20**, 831–835 (1969).
44. Smith, C. S. Grains, phases, and interfaces: An introduction of microstructure. *Trans. Met. Soc. AIME* **175,** 15–51 (1968).
45. Mullins, W. W. Theory of Thermal Grooving. *J. Appl. Phys.* **28**, 333–339 (1957).
46. Provatas, N. & Elder, K. *Phase-field methods in materials science and engineering*. (John Wiley & Sons, 2010).
47. DeWitt, S. & Thornton, K. Phase Field Modeling of Microstructural Evolution. In: Shin D., Saal J. (eds). in *Computational Materials System Design* 67–87 (Springer US, 2018).
48. Steinbach, I. Phase-field models in materials science. *Model. Simul. Mater. Sci. Eng.* **17**, 073001 (2009).
49. Emmerich, H. Advances of and by phase-field modelling in condensed-matter physics. *Adv. Phys.* **57**, 1–87 (2008).
50. Moelans, N., Godfrey, A., Zhang, Y. & Juul Jensen, D. Phase-field simulation study of the migration of recrystallization boundaries. *Phys. Rev. B - Condens. Matter Mater. Phys.* **88**, 1–10 (2013).
51. Moelans, N. A quantitative and thermodynamically consistent phase-field interpolation function for multi-phase systems. *Acta Mater.* **59**, 1077–1086 (2011).
52. Gentry, S. P. & Thornton, K. Simulating recrystallization in titanium using the phase field method. *IOP Conf. Ser. Mater. Sci. Eng.* **89**, 012024 (2015).
53. Gentry, S. P. & Thornton, K. Sensitivity analysis of a phase field model for static recrystallization of deformed microstructures. *Model. Simul. Mater. Sci. Eng.* **28**, 065002 (2020).
54. Hillert, M. On the theory of normal and abnormal grain growth. *Acta Metall.* **13**, 227–238 (1965).
55. Dennis, J., Bate, P. S. & Humphreys, J. F. Abnormal Grain Growth in Metals. *Mater. Sci. Forum* **558**–**559**, 717–722 (2007).
56. Burke, J. E. & Turnbull, D. Recrystallization and grain growth. *Prog. Met. Phys.* **3**, 220–292 (1952).
57. Urai, J. L., Means, W. D. & Lister, G. S. Dynamic recrystallization of minearls. *Miner. Rock Deform.* **36**, 161–199 (1986).
58. Rachinger, W. A. Relative grain translations in the plastic flow of aluminum. *Inst. Met.* **81** (1952).
59. Langdon, T. G. Grain boundary sliding revisited: Developments in sliding over four decades. *J. Mater. Sci.* **41**, 597–609 (2006).
60. Lifschitz, I. M. On the theory of diffusion-viscous flow of polycrystalline bodies. *Sov.*

Phys. **17**, 909 (1963).
61. Langdon, T. G. A unified approach to grain boundary sliding in creep and superplasticity. *Acta Metall.* **42**, 2437–2443 (1994).
62. Mullins, W. W. Magnetically induced grain-boundary motion in Bismuth. *Acta Metall.* **4**, 421–432 (1956).
63. Backofen, R., Elder, K. R. & Voigt, A. Controlling Grain Boundaries by Magnetic Fields. *Phys. Rev. Lett.* **122**, 126103-1–5 (2019).